CFD analysis and improvement proposals of a calorimeter for inline characterisation of solar concentrating collectors working fluids

Plamen Stefanov Avramov

plamen.avramov@tecnico.ulisboa.pt

Instituto Superior Técnico, Lisboa, Portugal

January 2021

Abstract

A revolution in renewable technologies has been underway for a couple of decades. In solar thermal energy, collector manufacturers have to test and certify their products following international standards. It is necessary to know precisely the specific heat (C_p) of the Heat Transfer Fluid (HTF) to calculate the power transferred. For thermal oils, this value is known with poor accuracy and degrades over time. To solve this problem, an in-line, measurement is of great importance. A calorimeter was developed in the past based on a temperature difference measurement when a known heating power is given to the fluid. In the present thesis, a detailed Computation Fluid Dynamics (CFD) simulation of this device was performed to access its design flaws and propose improvements. The simulations started by an iterative process keeping the balance between real system fidelity and computational time. In the validation, the C_p obtained was closer to the real value than in the experimental data since the simulation does not entail experimental uncertainties. An experimental measurement method flaw was identified caused by the lack of fluid mixing in the calorimeter's central chamber and a poor reading of the outlet temperature. The same simulation methodology was carried for synthetic oil in its expected operating temperature range of $230^oC - 320^oC$. Four geometries were proposed to potentially mitigate the problem by promoting fluid mixing in the central calorimeter zone. In two of the proposed geometries, the simulated C_p deviation is always below 3.9% for the imposed conditions.

Keywords: CFD, Calorimetry, Real-time C_p measurement, Steady-state flow calorimeter, HTF characterisation

1. Introduction

Global final[1] energy demand can be split into three main sectors, electricity, transportation and thermal energy every one of them corresponding to approximately 20, 30 and 50% of total world consumption, respectively. In 2018, 50% of the thermal energy demand was used in industrial processes, and another 46% was used in buildings. The thermal energy sector has contributed to 40% of global carbon dioxide (CO_2) emissions [2, 3].

High investments in solar Photovoltaic (PV), wind technologies and electric vehicles are making some progress in the de-carbonisation of the two first sectors, [4, 5]. Concentrating Solar Technologies (CST) have application potential for thermal energy, electricity production and, indirectly with the foreseen increase in electric mobility, in transportation.

Low and medium temperature collectors can be used in building HVACR[2] systems and industrial heat, respectively. Almost all medium and high-temperature collectors require solar radiation concentration and a Heat Transfer Fluid (HTF) to operate. These collectors produce steam or hot air which will be further used for industry heat and electricity generation using conventional power cycles. Presently, the most used ones are synthetic oils, but, for some time, there has been a transition to molten salts that allow higher temperatures and cycle efficiencies. It is essential to know the specific heat C_p of the fluids in both scenarios, so the collector or plant efficiency can be calculated.

Synthetic oils are preferred than water, despite the latter being a satisfactory and cheap HTF. Water would require very high working pressures for the desired operating temperatures.

Higher C_p values are appreciated in an HTF considering a lesser amount of fluid is required to transfer greater amounts of heat. Therefore, a detailed understanding of how HTF properties change during operation and the effects of continuous use in their thermophysical parameters is critical for CSC. Nevertheless, maintaining adequate C_p can be strenuous as synthetic oils degrade unpredictably with usage over time with significant losses beginning to arise.

Some literature solutions use calorimetric systems to mitigate the problem [6, 7]. The operation principle is based on a calorimeter placed inline with the HTF flow that allows real-time measurement of the fluid C_p. Understanding the physical parameters during operation would allow a correct estimation of the produced energy in a CSC system. This knowledge would also serve as a maintenance indicator avoiding further HTF and system performance degradation. It is essential having confidence in the measured C_p value during col-

---

[1]Final energy consumption is the total energy consumed by end-users, such as households, industry and agriculture. It is the energy that reaches the final consumer's door and excludes that used by the energy sector itself [1].

[2]Heating Ventilation Air Conditioning and Refrigeration

lectors characterisation, applying the appropriate test standards. Manufacturers have to report their collectors having particular efficiency, performance, which is obtained through testing. These tests are done using the energy yield, which is, in turn, dependent on the C_p value.

2. State of the Art

2.1. Calorimetry

Calorimetry is the activity associated with determining a system's energy changes by measuring the heat exchanged with its surroundings. The device used to measure the quantity of heat transferred to or from an object is called a calorimeter [8].

The specific heat is depicted either as a ratio between heat Q transferred to any material and its mass m. Alternatively, as a ratio between power $\dot{Q}$ transferred to the material and its mass flow rate $\dot{m}$, given a temperature gradient, left and right-hand side of Equation (1), respectively. For a broader temperature range, specific heat of a substance as a function of temperature $C_s(T)$ has to be considered.

$$C = \frac{1}{m}\frac{\delta Q}{dT} = \frac{1}{\dot{m}}\frac{\delta \dot{Q}}{dT} \qquad (1)$$

During measurements, fluid is kept at constant volume as incompressible liquids constant volume and constant pressure specific heats are equivalent. As we will be working with a fluid that can be considered incompressible, the specific heat is commonly written as C_p, and this notation will be carried on.

An extensive literature review was carried out for the different technologies and devices, of which a list follows.

- Adiabatic Calorimeter

- Reaction Calorimeter

- Isothermal Calorimeter

- Calvet Calorimeter

- DSC Calorimeter

- Flow Calorimeter

From the presented list of existing calorimeters in the literature, just the last two are used in CST applications, namely, Flow and Differential Scanning Calorimetry (DSC) types.

Differential Scanning Calorimeter

Differential Scanning Calorimeters do not allow real-time synthetic oil properties measurement. However, their high-temperature range of operation, up to $500^o C$, makes them very important and widely used for high precision measurement of $C_p(T)$ in CSC systems. The principle of specific heat C_p measurements consist of heating a blank, the sample and a reference material through the same temperature range at a fixed rate in a controlled environment [9].

A good practice for accurate value measurement is demonstrated in [10] where DSC is occasionally used alongside flow calorimeter results, aiding their validation. A DSC allows gradual step heating of the sample in a relatively big span of temperatures and pressures, including the temperature range of operation of most CSC systems.

Flow Calorimeter

The principle of a flow calorimeters is measuring as precisely as possible a differential temperature ($T_{out} - T_{in}$) heated by an electrical resistor power dissipation P_R. This system is placed in a mass flow loop, and additional mass flow rate $\dot{m}$ measurement enables C_p calculation. There has been some variety of flow calorimeter design reported in several papers over the years. Nevertheless, a basic measurement setup is shown in Figure 1, with C_p measurement directly derived by Expression (2).

$$C_p(T) = \frac{P_R}{\dot{m}(T_{out} - T_{in})} \qquad (2)$$

Flow calorimeters aim to reduce thermal losses as much as possible, where achieving zero thermal losses would be a perfect case scenario. In that case, a lossless flow calorimeter system could also be considered an adiabatic one as heat exchange would not occur to the surroundings. The value of the differential temperature ΔT will be strongly dependant on the mass flow rate $\dot{m}$ and the resistive power P_R given to the fluid. Higher mass flow fluids will spend less time passing around the heater, hence receiving less heat and lesser power means lesser temperature increment.
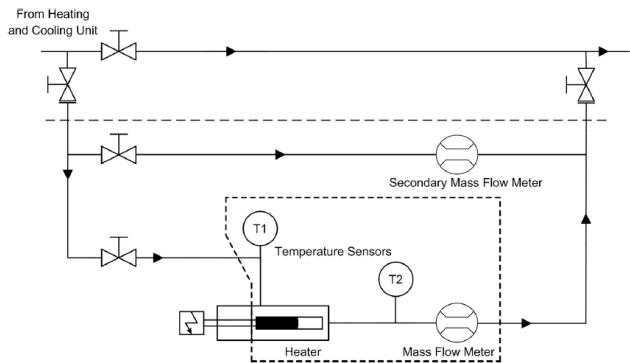

Figure 1: Basic piping diagram of the flow through calorimeter setup, from [10], indicating the measurement section (dashed box), the heater, the mass flow meter, the temperature measurement locations and the flow direction.

2.2. Heat Transfer Fluids (HTF)

The HTF is one of the critical components for overall performance and efficiency of concentrating solar systems. The HTF can be used to directly drive a turbine, in case of air being used as HTF, to produce power or, more commonly, be combined with a heat exchanger and a second cycle to generate steam. Since a large amount of HTF is required for CST to operate, it is necessary to minimise its cost while maximising its performance.

Besides transferring heat from the receiver to the steam generator, heated HTF can also be stored in an insulated tank for power generation when sunlight is not available [11].

The HTF's thermal stability is essential as it is the fluid resisting to chemical degradation at high temperatures. The selection process of an HTF requires [12–14], characterisation of some thermophysical and rheological[3] properties. The effect of this characterisation is going to be crucial for the selection of some fundamental system factors, namely heat exchanger size, pumping consumption, or vessels pressure rating [14]. In [13], four different thermophysical and rheological parameters are discussed and analysed as the most important ones.

- Density ρ

- Thermal conductivity k

- Specific heat C_p

- Dynamic viscosity μ

The degradation of HTF for CSC operating temperatures is reviewed in [16, 17]. The first paper shows that aged fluid samples, with two years of operation, demonstrate inferior performance than new ones, losing up to 30% of their C_p at higher operational temperatures. The same paper stresses that new transfer fluid C_p can be up to 25% lower than the one provided by manufacturers, at higher operating temperatures. In other words, the system calculations will be wrong, and adjustment of the flow will be required to secure the desired ΔT. This mass flow rate $\dot{m}$ adjustment has to be made with an actual C_p and could lead to additional pumping costs.

3. Simulation Implementation

3.1. Computational Fluid Dynamics

CFD is a branch of fluid mechanics that produces quantitative predictions of fluid-flow phenomena based on the conservation laws (conservation of mass, momentum, and energy) governing fluid motion [18]. The numerical simulations are an alternative to physical experiments and can be very valuable in situations where experiments can be challenging to execute in practice. Additionally, these simulations can be instrumental in conceiving and refining whole systems a priori to eventual manufacturing. The modelling software chosen for the system was *Solidworks* [19] as it is vastly used and well documented. Another reason for this choice was the CAD compatibility with the CFD software for this thesis, namely, *Ansys Fluent* (AF) [20].

CFD is based on the three fundamental equations of fluid dynamics: continuity, momentum, and energy. These equations are based on three physical principles [21]:

- **Conservation of Mass:** Continuity Equation

- **Conservation of Momentum:** Newton's Second Law

- **Conservation of Energy:** First Law of Thermodynamics or Energy Equation

This scientific field originally developed based on new approaches to solving the Navier Stokes (NS) equation numerically. One advantage of CFD is that it can process an immense amount of data, which would be impossible without computational aid.

3.2. Geometric model and Meshing

Geometric model

Relying on existing technical drawings in [22] and direct measurements provided by [23] an identical geometry for the calorimeter system was modelled in *SolidWorks*. Figure 2 presents a much cleaner version, details-wise, of the geometry presented in [7], being this way more adequate for a CFD simulation.
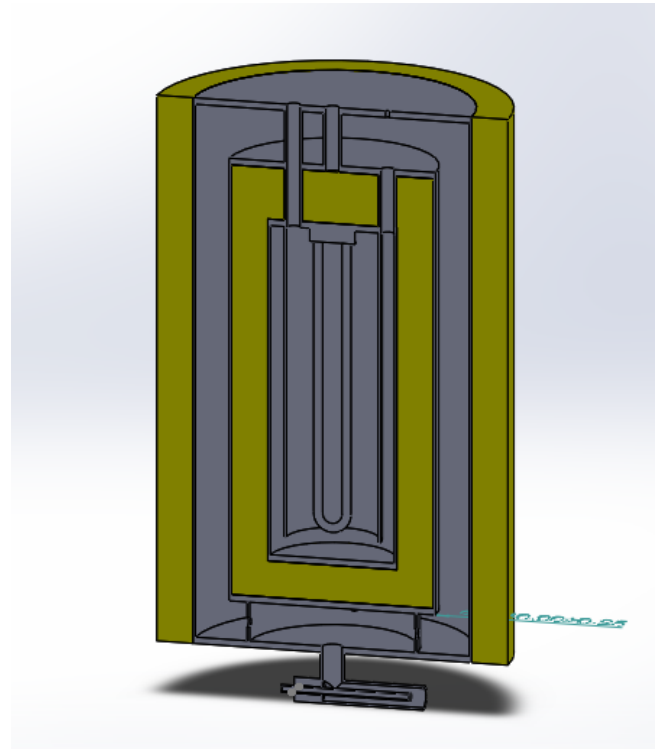

Figure 2: Cross section of the calorimeter geometry modelled in Solidworks.

Probes insertion

Three different probes were used, one large and two smaller ones, in the system described in [7], and this thesis. The probes are high precision RTD[4] with platinum resistance (4wire-PT100) and a stainless steel thermowell. The larger, $6\,mm$ in diameter probe, is placed at the entrance of the calorimeter. Whilst, the two smaller ones, $3\,mm$ in diameter probes, are placed at the inlet and the outlet of the calorimeter's *IC*.

3.2.1 Meshing

Applying all the conservation equations previously mentioned all over an entire system is impossible. This is why having planned, segmented and sequenced tasks

---

[3]Rheological properties are the properties that rule the way material deform or flow in response to applied forces or stresses. [15].

[4]Resistance Temperature Detector

has been the key for CFD simulations. To conduct an analysis, the solution domains are split into multiple sub-domains called cells and are where calculations will be made. The combination of these cells in the computational structure is named grid or mesh, and it is a discrete representation of the geometry [21, 24]. Mesh generation process is crucial to obtain reliable solutions. A quality mesh improves numerical stability and increases the solution's validity being intrinsically connected to the rate of convergence. This stability is the reason why some regions are more important than others and require finer mesh. Doing an ever more detailed grid with the number of elements tending towards infinity comes at an increasingly higher computational cost.

3.2.2 Mesh quality and convergence

Errors based on mesh structure are often a struggle that results in simulation failure. Overly coarse grids do not cope with all effects happening in a single cell element one by one. By getting a finer mesh, dealing with multiple effects becomes easier. Therefore, the accuracy of the solution enormously depends on the mesh structure [21].

A brief description of some of the essential mesh metrics and their respective recommended ranges follows.

1. Aspect Ratio - Aspect ratio does not have a well-defined range in which simulation results are guaranteedly inferior but provides value recommendations depending on the system.

2. Orthogonal Quality - The orthogonal quality metric ranges from 0 to 1, bad and good, respectively [25].

3. Skewness - A value of 0 indicates a best-case equilateral cell and a value of 1 indicates an entirely degenerate cell.

4. Smoothness - It is more subjective metric than the others as it is not intricate to each cell. Smoothness is the change in adjacent cells' size, and it should be as gradual as possible (smoother).

In [24], the recommended mesh metrics to follow are the aspect ratio, and the skewness, as the low-quality grid will cause inaccurate solutions and slow convergence. In the context of this master thesis, extreme care was taken for the grid skewness and aspect ratio when performing the meshing convergence process.

The elected final grid complies with all the, previously mentioned, quality recommendations apart from the orthogonal quality, whose minimum value is below the recommended 0.15. Despite that fact, the number of elements below this threshold was maintained low, having just ten out of approximately six million. Additionally, these cells are located out of the fluid domain's critical zone and do not interfere with the simulation results.

3.2.3 Mesh independence study

Having a converged solution is not necessarily a correct one despite being a good indicator. The precision of the simulation results will have an asymptotic behaviour, i.e., additional mesh improvement will not improve the simulation result linearly, but just by smaller and smaller amounts with every further improvement. In simulations with scarce experimental data available, it is recommended to perform a mesh independence study at least once for a given problem allowing more confidence in the results [26]. The mesh independence study's main goal is to improve the mesh to a point where further refinement would not substantially change/improve the simulation results.

There are some zones more critical than others inside the calorimeter system, namely, around both probes. A temperature difference tolerance of $0.1^{o}C$ was considered for the three studied grids A, B and C, each being finer than the last, respectively. For one of them to be considered independent from another, no temperature difference, larger than the imposed tolerance could be revealed in the temperature plots made for all critical zones. A thorough analysis was carried for the outer probe, where more considerable temperature differences were expected. It was concluded that grid A is not independent of the rest, however, grid B was considered independent from C, with some additional considerations. For water simulations, the temperature difference was about half of the imposed tolerance, while it was approximately equal to $0.1^{o}C$ for synthetic oil simulations.

3.2.4 Heat transfer

The software AF is equipped with the three known mechanisms by which heat may flow: conduction, convection, radiation. The conduction and convection models provided by AF do not require additional analysis, so only the radiation process modelling will be addressed during the thesis.

Modelling radiation

The AF software provides five radiation models, with or without participating medium, that allows the inclusion of radiation in heat transfer simulations. A radiation model should be included whenever the radiation heat flux is not negligible compared to the heat transfer due to convection or conduction. Furthermore, another model is included that allows the inclusion of solar radiation in the simulations. For specific problems, one radiation model may be more appropriate than others.

1. Discrete Transfer Radiation Model (DTRM)

2. Discrete Ordinates Model (DO)

3. P-1 Model

4. Rosseland Model

5. Surface to Surface Model (S2S)

Initially, all three transport mechanisms were included. All water simulations were modelled using the S2S radiation model considering non-participating media. After performing high-temperature simulations with synthetic oil, it was confirmed that radiation has residual effects compared to conduction and convection. In other words, having the radiation model enabled or disabled makes no difference in the results. Lack of detailed information about the optical properties of *Castrol Perfecto HT5* and considerably longer simulation

times lead to the disabling of radiation models for the rest of the simulations.

3.3. Turbulence

The first thing to do once dealing with flows is to perform estimation to understand whether the flow is laminar or turbulent. The Reynolds number is a ratio of inertial to viscous forces and is a convenient parameter for predicting if a flow condition will be laminar or turbulent [27].

$$Re = \frac{\text{inertia forces}}{\text{viscous forces}} = \frac{\rho v D_H}{\mu} \qquad (3)$$

Where v is the velocity of the flow, D_H is the characteristic linear dimension or hydraulic diameter, ρ is the fluid density, and μ is its viscosity. There are, in general, three types of internal fluid flow, laminar, transitional and turbulent [28].

Initial estimations for Re in the system reveal the flow is laminar nearly everywhere with some exceptions. According to these estimations, the laminar model would be the most suitable for the AF system; however, after several test simulations, always unsatisfying results were retrieved. This behaviour is explained by the fact that the laminar model behaves accurately only in highly isotropic geometries, not the case for this system. Direction gradients and obstacles can be considered disturbances of the flow which may cause a transition to turbulence at lower Re [29]. This transition will generate local turbulence causing both laminar and turbulent flows to coexist in the system. The latter is better modelled by a stable turbulence model.

3.3.1 Modelling turbulence

Unfortunately, there is not a single turbulence model excelling in every type of simulation. The software AF offers a vast choice of turbulent flow models, so, an extensive literature review was carried about them and their properties.

Turbulence model selection was primarily narrowed down through computational demand which led to a few Reynolds-averaged Navier-Stokes (RANS) models. The one model that showed the most promising and physically accurate results, after performing test simulations, was the standard $k - \epsilon$ model. It is a model known for its computational economy, robustness, and reasonable accuracy for a wide range of turbulent flows.

Unfortunately, there is not a single turbulence model excelling in every type of simulation. The software AF offers a vast choice of fluid flow models, mostly turbulent, and their variations. Follows some analysis of how the turbulence models are categorised and which ones constitute the most interest for this project.

3.4. Simulation

The first set of simulations was performed to compare with existing experimental data provided by [23]. The experimental data provided is the average of several measurements made for the C_p water calculation under distinct conditions. This set also serves as validation for the simulation conditions by seeing how it approximates to real-life measurements. The following control parameters were used for the simulation initial conditions:

- T_{IN} - Inlet Temperature

- $\dot{m}$ - Mass flow rate

- C_p - Specific heat

- P_R - Electrical Power

The high uncertainty present in C_p calculation for the provided data compared difficultly to a simulated C_p. Other quantities were also used as reference points to validate the simulation: The temperature at the inlet T_{in} and at the outlet of IC T_{out}. These correspond to the temperatures measured by the two $3\,mm$ probes, placed at the inlet and outlet of the IC. The temperatures were obtained by sampling the average temperature of the sensitive area of the simulated probes. This area consists of the horizontal tip surface and a $2\,cm$ tall surface surrounding the probe near the tip. This area was considered to have perfect thermal contact with the real-life probe's sensitive part, thus having the same measured temperature.

3.4.1 Additional parameter measurements

After performing multiple simulations, there were some difficulties in reading the results. Therefore additional parameters were introduced to improve the simulation analysis.

Expected Experimental Uncertainty

The provided data made possible computing the expected experimental uncertainty of the C_p measurement considering two different sources.

1. Statistical uncertainty - The provided experimental data measurements were performed in a stable system, near steady-state. These measurements were made over time, and just like any other real-life experiment presents some oscillations. Statistically analysing, both average value, x, and standard deviation, σ, were obtained for every given parameter.

2. Apparatus calibration uncertainty - Every device used during experimental tests comes with a calibration uncertainty provided by its respective manufacturer. Considering the uncertainty values provided by the manufacturers are maintained constant over time.

These parameters would help identify the most significant experimental uncertainty source and its value if the performed simulations were a real-life measurement. In other words, every C_p value outside of this range will have an additional, possibly unaccounted for, sources of uncertainty. The expected experimental uncertainty associated to the apparatus will be denoted as δ_{ea} while the one associated with the system oscillations will be δ_{eo}.

Mass flow weighted average temperature

The Mass Flow Weighted Average ($mfwa$) temperature is measured on the cross-sections of the inlet and outlet of the IC. This parameter will describe the average temperature at the section, as faster-moving fluid will weigh more than the stagnated one. Further, C_p calculated value will be more reliable and can be denoted as the target C_p. Simulated C_p deviation Comparing both C_p values obtained through the simulation, via $mfwa$ temperature, and via probe temperatures, will result in the simulated C_p deviation.

4. Results

4.1. Water simulations

4.1.1 Simulation validation

Water simulations were performed, imposing a constant C_p value to AF. Operation temperature T_{IN}, mass flow rate $\dot{m}$ and resistive power P_R were also used as initial conditions. The imposed constant C_p values were obtained through the average experimental probe temperatures, T_{in} and T_{out}, in the experimental data set. The first set of simulations consisted in twelve separate scenarios for different temperatures and mass flow rate.

There are two separate C_p values computed along all the performed CFD simulations:

1. The first one is the $C_{p-simulated}$ computed using the simulated temperature at both inlet T_{in} and outlet T_{out} probes. This C_p is computed through Equation (4).

$$C_{p-simulated} = \frac{P_R + IC_{loss}}{\dot{m}\Delta T_{IC}} \qquad (4)$$

With IC_{loss} being the integrated thermal losses of the IC, and ΔT_{IC} the temperature difference of the IC computed with temperatures obtained at both probes.

2. The second one is the C_{p-mfwa} computed using the mass flow weighted average temperature, hence the $mfwa$ subscript, at the sections entering and exiting the IC. In other words, this C_p is computed using Equation (4) as well, nevertheless, using a different ΔT. Despite also being a simulated value, it corresponds to the actual amount of heat transferred to the fluid by the heater and shall not be confused with the first one.

The simulated C_p deviation denoted as δ_p, presented in all future simulations, is obtained using both simulated C_p variables through Equation (5).

$$\delta_p(\%) = \frac{|C_{p-mfwa} - C_{p-simulated}|}{C_{p-mfwa}} \times 100\% \qquad (5)$$

Using an imposed constant C_p value for the water simulations allows an additional validity check between the imposed one and the obtained through $mfwa$ temperature. This comparison is denoted as simulation deviation δ_s and verifies how close is the $mfwa$ temperature

obtained C_p to the constant imposed value. The simulation deviation δ_s is computed through Equation (5) performing the necessary C_p replacements.

For the first water simulations set, the obtained simulation deviation was always $\delta_s < 0.6\%$, which is a good indicator for simulation validity. Low simulation deviation δ_s values show that the AF model is self-consistent, and the internal calculations are working well. Both simulated C_p values, probe ΔT, $\delta_p = [0.7, 9.3]\%$, and $mfwa$, $\delta_s = [0.1, 0.6]\%$, are multiple times closer to the actual amount than the obtained experimentally $\delta_{exp} = [14.7, 35.8]\%$[5]. This result suggests the simulation is computing better results than the real-life measurements, which is, in fact, entirely reasonable. The simulation has no associated uncertainties to the apparatus, and a converged result in AF is an assurance for a steady-state system.

Therefore, assuming the model is self-consistent implies that it was correctly implemented corroborating the simulation validity and further analysis.

The experimental data set presents high uncertainties related to the measurement equipment and system fluctuations. These uncertainties will lead to C_p results significantly deviating from the exact value. Nevertheless, the estimated experimental uncertainties are far from comprising the correct C_p value in its confidence range. On top of these uncertainties, further fluid and energy analysis through the simulation will reveal a problem in the method of T_{out} measurement, providing even worse results.

The simulation not accounting to experimental uncertainties means that any difference between simulated C_p deviation δ_p and simulation deviation δ_s will account for the problem existing in the experimental results. In other words, the C_p obtained through $mfwa$ temperature measurement is the target C_p value that one needs. In contrast, the C_p obtained through probe temperature measurement is associated with the method problem.

This problem associates with a poor fluid mixing in the IC that will lead to a flow with a stratified temperature near the output probe. This heterogeneity around the outer probe will cause the temperature measurement, thus calculated C_p, to deviate significantly from the exact value.

4.1.2 Partial probe extraction simulations

From the initial water set simulations, four different scenarios were run with partial extraction of the outer probe $30mm$, to check if there is an improvement in the temperature measurement. Despite no adding additional mixing to the IC, extracting the outer probe slightly, opens some space for additional mixing in the pipe leaving the calorimeter before reaching the probe. The end-goal is to obtain a computed C_p value through the probes temperature difference as close as possible to the target C_{p-mfwa}.

This approach caused reduction in the simulated C_p deviation $\delta_p = [0.6, 4.0]\%$ for the four simulated scenarios. Additionally, it was concluded that the IC losses have residual values $< 0.5\%$ when compared to the heat provided by the resistance.

---

[5]Existing outlier at 97.5%

4.2. Thermal oil simulations

Once the simulation is validated, CFD simulations were performed with *Castrol Perfecto HT5* synthetic oil at usual CSC operating temperatures $(230-320^oC)$. Instead of using a constant C_p value for each scenario, a tabulated C_p values were used, making the simulation more realistic. As there is no more constant C_p value in the simulation, simulation deviation δ_s will no longer be used for oil measurements.

The same proceeding as for the water simulations was followed. First set of twelve different scenarios with a fully inserted probe, followed by four scenarios with the outer probe extracted by $30mm$. The first set displayed significant temperature flow heterogeneity, on both sides of the probe, translating into an erroneous measurement of the probe and, as a result, high simulated C_p deviations $\delta_p = [9.3, 47.6]\%$.

For the smaller set, a better C_p value was computed with significantly reduced simulated C_p deviation $\delta_p = [4.9, 10.1]\%$ on almost all of them. Figures 3 and 4 compare temperature profile around the outer probe for fully inserted and slightly extracted probe, respectively. The first displays significantly larger ΔT around the outer probe when compared to the second. Both figures correspond to case 11 which runs with operation temperature $T_{IN} = 320^oC$ and mass flow rate $\dot{m} = 0.049kg/s$. The other three cases from the slightly extracted probe set display similar behaviour regarding fluid temperature homogeneity. This set will be used as a reference for the proposed geometries section considering they display better results than with a fully inserted probe.
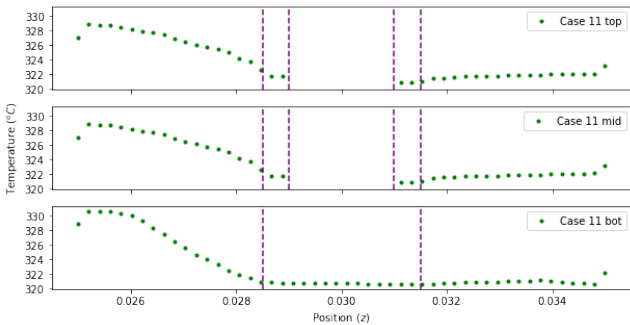

Figure 3: Probe lines exhibiting fluid temperature behaviour around outer probe, normal case 11, synthetic oil.

4.2.1 Mixing promoters insertion

This section aims to model, simulate, and analyse several types of geometries that will help promote turbulence and mixing in the *IC* or, at least, before the outlet temperature sensor, by inserting them into the system.

Single oblique barrier

The purpose of the single oblique barrier is to channel the fluid flux closer to the heater. The existence of obstacles in the fluid promotes local turbulence, which will improve mixing and homogenisation in the *IC*. All four scenarios exhibit considerably improved results when
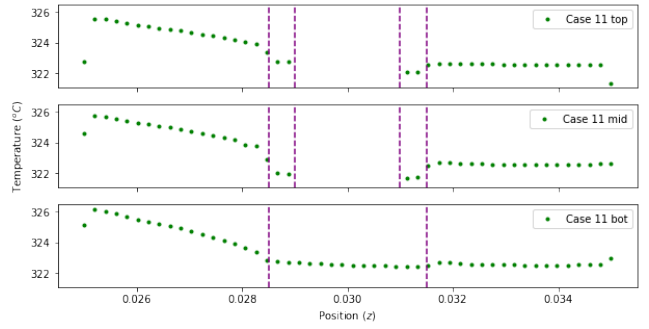

Figure 4: Probe lines exhibiting fluid temperature behaviour around outer probe, extracted probe case 11, synthetic oil.

compared with the reference values, now with simulated C_p deviation $\delta_p = [0.2, 2.9]\%$.
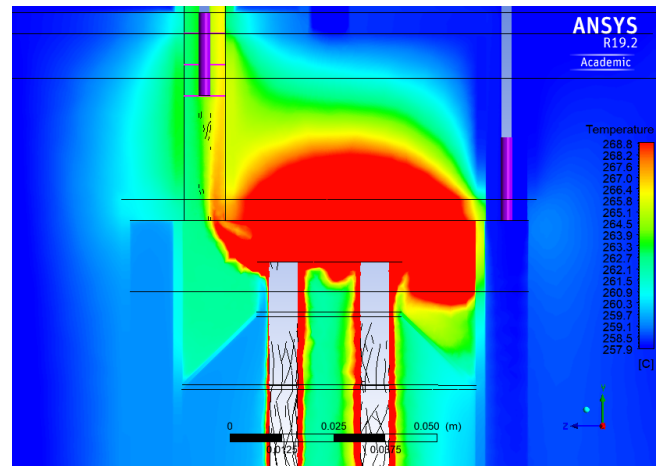

Figure 5: Temperature cross section of calorimeter *IC* upper part, for case 5 with single oblique barrier, synthetic oil.

Figure 5 exhibits a generally warmer area above the oblique barrier compared to a simulation without an existing one. Additionally, the fluid being narrowed near the heater certifies no unheated fluid is heading directly to the outlet. This additional convergence of the flow to the middle promotes local turbulence in the *IC* generating extra mixing.

Double oblique barriers

After analysing the single oblique barrier results, it was clear there was an improvement given more homogeneous flow around the outer probe and lower simulated C_p deviation δ_p. Although, there was still fluid going directly from the heater to the *IC*'s outlet with mostly laminar flow. This steady flow birthed the idea of having a second oblique barrier. The second one would diverge the flow outwards and upwards of the *IC* while mixing it in the meantime.

Despite doing well for a case that previously had a bad result, this approach saw worse outcome for the other 3 with simulated C_p deviation $\delta_p = [1.5, 14.2]\%$. Having a second oblique barrier with approximately the same length as the first one left little room for the flow to pass
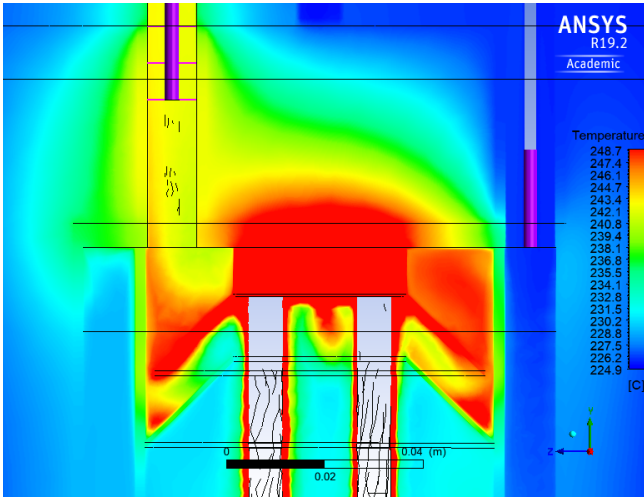
Figure 6: Temperature cross section of calorimeter IC upper part, for case 1 with double oblique barrier, synthetic oil.

accelerating it near the wall and retrieving worse results for faster flows. This acceleration near the border caused the flow to be less turbulent in the last section before the outlet, maintaining the hotter fluid near the wall. With the less mixed, hotter fluid near the border, far from the centred probe, inaccurate results are retrieved for higher mass flow rates $\dot{m}$.

Horizontal + oblique barriers

The idea for this approach came after analysing the results for a single oblique barrier. The tunnelling it provides to the heater area allows using a second barrier deviating the flow from immediately exiting the IC. The double oblique barrier results revealed that leaving too little space for the fluid to pass through near the wall can harm the probe temperature measurement.
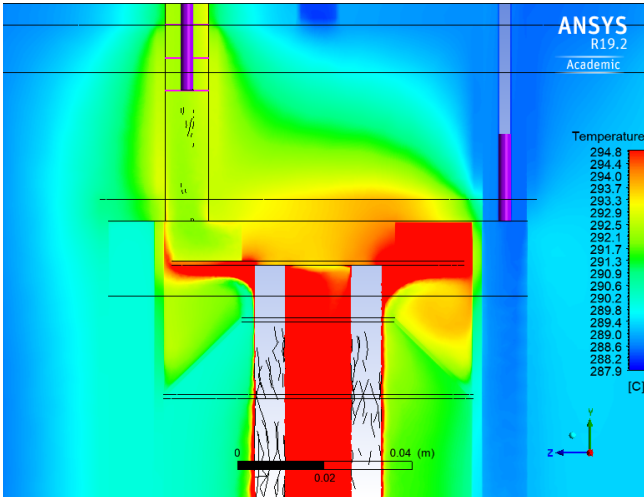

Figure 7: Temperature cross section of calorimeter IC upper part, for case 9 with horizontal + oblique barrier, synthetic oil.

The temperature profile of Figure 7 gives a glimpse of a very well mixed fluid in the outer probe's vicinity. This approach displays some promising and consistent

results for almost all the scenarios. Apart from case 11, $\delta_p = 3.9\%$, which showed slightly worse outcomes, the simulated C_p deviation values are always $\delta_p < 2\%$.

Revised Double oblique barrier

After retrieving the results from simulations with double barrier was clear that adding the second, top, barrier with the same size as the first would excessively force the flow to the IC walls causing laminar flow once again. This excessive squeezing of the flow up the IC walls motivated the length reduction of the second oblique barrier to about half its original size. This modification was expected to cause a smoother separation of the flow outwards after being initially converged to the heater by the first one, especially for higher mass flow rates.
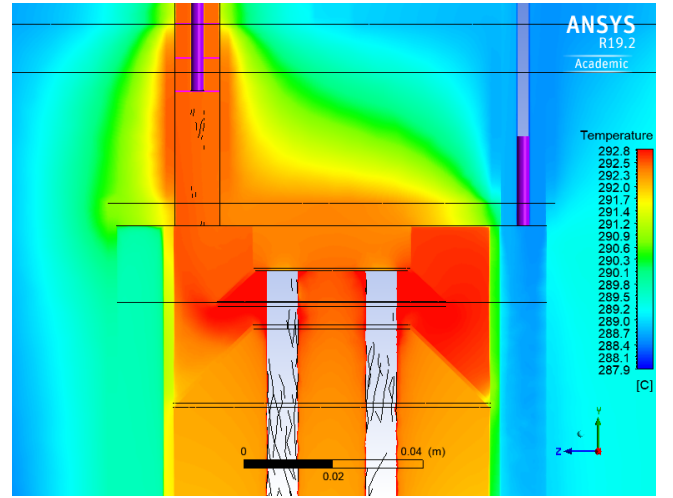

Figure 8: Temperature cross section of calorimeter IC upper part, for case 9 with revised double oblique barrier, synthetic oil.

Figure 8 exhibits one of the most homogeneous temperature contours as this outcome is given by the well-mixed flow, which in turn is enabled through local turbulence. The flow has a longer path between the heater and the sensitive part of the outer probe but has no unnecessary acceleration resulting from compression near the wall. This approach provided possibly the best outcome with all cases apart from 11 having simulated C_p deviation $\delta_p < 0.4\%$. Only case 11 provided slightly worse result with simulated C_p deviation $\delta_p = 3.3\%$, in line with the horizontal + oblique approach.

4.2.2 Proposed geometries overview

Table 1 compares all proposed geometry results along with the slightly extracted probe serving as a reference.

Apart from the double oblique barrier results, every proposed geometry exhibited an improvement in temperature homogeneity around the probe and C_p measurement through probe temperatures.

Single oblique barrier presents some very low simulated C_p deviation values. This outcome suggests that this simple geometry might be amongst the most suitable options to mitigate the problem; however, this data can be misleading.

8

Table 1: Proposed geometries overview. Comparison of simulated C_p deviation $\delta_p(\%)$ for slightly extracted probe and all four proposed geometries.

Case	Slightly extracted probe	Single oblique barrier	Double oblique barrier	Oblique + horizontal	Revised double oblique
1	4.9	2.9	1.5	0.3	0.1
5	10.1	1.9	14.2	1.8	0.0
9	6.7	0.2	8.4	1.2	0.4
11	9.9	0.9	13.4	3.9	3.3

Despite being better than the reference, the temperature profiles around the probe for this approach still reveal some fluid temperature heterogeneity present. The little mixing in the IC leads to an average integration that results in a C_p calculation very close to the exact value (lucky run), hence the low δ_p. Observing the fluid temperature behaviour of the horizontal + oblique and revised double oblique barriers can conclude this is not the case for these approaches. The temperature cross-sections of the IC, Figures 7 and 8, and their respective fluid temperature behaviour around the outer probe, proves the low simulated C_p deviation values, for theses geometries, are not caused as a result of a lucky run.

Considering the initial goal was to minimise the simulated C_p deviation of the simulation through better flow mixing, the final verdict is the revised double oblique barrier. This geometry simulated C_p deviation is less than 0.5% for three out of the four simulated scenarios with its worst result being at the highest operating temperature.

5. Conclusions and Future work

All C_p values obtained during simulation validation were far closer to the actual amount than the experimental results hence validating the simulation. The leading cause of this outcome is that simulation does not carry either apparatus or oscillation uncertainties in its results. After the first analysis, an unexpectedly substantial temperature disparity around the outer probe was revealed. This method measurement flaw came to explain the significantly higher than real C_p values, measured, as some of the results were far outside the confidence range of estimated experimental uncertainties. The method deficiency is caused by a lack of mixing in the IC, resulting in inaccurate C_p outcome. The same simulations, repeated with a slightly extracted outer probe, retrieved better results. Simulated C_p deviation is always $\delta_p < 4\%$ for simulations with water and slightly extracted probe.

The same methodology was applied for simulations with *Castrol Perfecto HT5* as HTF but this time for a more typical calorimeter operating temperature, $T_{IN} = 230 - 320^o C$. Regardless of its overall higher simulated C_p result, synthetic oil simulations displayed the same behaviour—substandard results for fully inserted probe, and significantly better ones for simulations with a slightly extracted outer probe. The four scenarios with the partially extracted probe were used as a reference for simulations with additional geometry that would promote mixing in the IC and compute better results. Four different geometries were proposed with the last two, horizontal + oblique and revised double oblique, providing better results. Both approaches provide satisfying simulated C_p deviations, for cases 1, 5 and 9, with $\delta_p < 1.8\%$ and $\delta_p < 0.4\%$, horizontal + oblique and revised double oblique, respectively. Nevertheless, it is the last iteration approach that exhibits results accurate enough to be used in future calorimetry projects.

The initial idea was that better insulation was required for the calorimeter having significant losses in mind. Results from both water and synthetic oil simulations exhibited losses of the IC always lesser than 0.5% of the resistive power P_R provided by the heater. The IC losses had consistently the same order of magnitude for temperature ranging $55-330^o C$ with this result proving the calorimeter was thermally well-conceived from the beginning. Placing the IC and OC in series while thermally shielded by the second, makes the losses of the first independent from the difference between ambient and fluid temperature.

When performing a CFD simulation for similar applications, high-performance machines and parallel processing are recommended for better outcomes and sparing significant amounts of time. The already elevated number of elements in the grid had to be considered while modelling the turbulence promoters. More complex geometries would require higher mesh resolution for proper simulation, which was impossible with the current setup.

References

[1] Final energy consumption definition. https://ec.europa.eu/eurostat/statistics-explained/index.php/Glossary:Final_energy_consumption, Accessed December 10, 2020.

[2] REN21. Renewables 2020 global status report. REN21 Renewables Now, 2020. URL https://www.ren21.net/wp-content/uploads/2019/05/gsr_2020_full_report_en.pdf.

[3] IEA (2019). Renewables 2019 - heat. IEA, Paris, Accessed December 23, 2019. URL https://www.iea.org/reports/renewables-2019.

[4] IRENA (2019). Future of wind. IRENA, Accessed January 11, 2020. URL https:

//www.irena.org/-/media/Files/IRENA/
Agency/Publication/2019/Oct/IRENA_Future_
of_wind_2019.pdf.

[5] IEA (2019). Global ev outlook 2019. IEA, Paris, Accessed January 11, 2020. URL https://www.iea.org/reports/global-ev-outlook-2019.

[6] Christoph Hilgert, Gregor Bern, and Marc Röger. Kontas-CP - Flow Through Calorimeter for Online Heat Capactiy Meausrement of Thermal Oils in CSP Applications. *Solar Energy*, 2012.

[7] J. Marchã, T. Osório, M. Collares Pereira, and P. Horta. Development and test results of a calorimetric technique for solar thermal testing loops, enabling mass flow and Cp measurements independent from fluid properties of the HTF used. *Energy Procedia*, 2014. doi: 10.1016/j.egypro.2014.03.225.

[8] Calorimeters and calorimetry. https://www.physicsclassroom.com/class/thermalP/Lesson-2/Calorimeters-and-Calorimetry, Accessed December 24, 2020.

[9] Judith C. Gomez, Greg C. Glatzmaier, and Mark Mehos. Heat capacity uncertainty calculation for the eutectic mixture of biphenil/diphenyl ether used as heat transfer fluid. *National Renewable Energy Laboratory (NREL)*, 2012.

[10] Christoph Hilgert, Fabian Howar, and Marc Röger. Flow through calorimeter to measure fluid heat capacity in CSP applications. *Solar Energy*, 2019. URL https://doi.org/10.1016/j.solener.2019.11.029.

[11] K. Vignarooban, Xinhai Xu, A. Arvay, K. Hsu, and A. M. Kannan. Heat transfer fluids for concentrating solar power systems - A review. *Applied Energy*, 2015. URL http://dx.doi.org/10.1016/j.apenergy.2015.01.125.

[12] Eric Serge Kenda, Kokouvi Edem N'Tsoukpoe, Igor W.K. Ouédraogo, Yézouma Coulibaly, Xavier Py, and Fabrice Marie Armel W. Ouédraogo. Jatropha curcas crude oil as heat transfer fluid or thermal energy storage material for concentrating solar power plants. *Energy for Sustainable Development*, 2017. URL http://dx.doi.org/10.1016/j.esd.2017.07.003.

[13] J. F. Hoffmann, G. Vaitilingom, J. F. Henry, M. Chirtoc, R. Olives, V. Goetz, and X. Py. Temperature dependence of thermophysical and rheological properties of seven vegetable oils in view of their use as heat transfer fluids in concentrated solar plants. *Solar Energy Materials and Solar Cells*, 2018. doi: 10.1016/j.solmat.2017.12.037.

[14] Aboubakar Gomna, Kokouvi Edem N'Tsoukpoe, Nolwenn Le Pierrès, and Yézouma Coulibaly. Review of vegetable oils behaviour at high temperature for solar plants: Stability, properties and current applications. *Solar Energy Materials and Solar Cells*, 2019. URL https://doi.org/10.1016/j.solmat.2019.109956.

[15] Ludger O.Figura and Arthur A.Teixeira. *Food Physics Physical Properties — Measurement and Applications*. Springer, 2007. doi: 10.1007/978-3-540-34194-9.

[16] Héctor Barroso, Francisco Sanz, Miguel Hernández, Daniel Pereira, Daniel Rayo, and Enrique Serrano. Understanding of the htf degradation on parabolic trough power plant energy performance. *Sun to Market Solutions*, 2012. URL http://cms.solarpaces2012.org/proceedings/paper/f6c74f102003b7cea33c9759f32c1f4.

[17] C. Lang and B. Lee. Heat Transfer Fluid Life Time Analysis of Diphenyl Oxide/Biphenyl Grades for Concentrated Solar Power Plants. *Energy Procedia*, 2015. doi: 10.1016/j.egypro.2015.03.077.

[18] H. H.. Hu. Computational Fluid Dynamics. Fluid Mechanics. *Elsevier Inc.*, page 421–472, 2012. doi: 10.1016/b978-0-12-382100-3.10010-1.

[19] Solidworks. https://www.solidworks.com/, Accessed December 2, 2020.

[20] Ansys fluent cfd. https://www.ansys.com/products/fluids, Accessed December 2, 2020.

[21] What is cfd — computational fluid dynamics? https://www.simscale.com/docs/simwiki/cfd-computational-fluid-dynamics/what-is-cfd-computational-fluid-dynamics/, Accessed November 2, 2020.

[22] João Paulo da Cruz Marchã. Conceção, construção e ensaio de um calorímetro para bancos de ensaio de coletores solares a temperaturas entre 100º c e 200º c. Master's thesis, Universidade de Évora, 2016.

[23] Tiago Osório. personal communication, January to November 2020. URL tiagoosorio@uevora.pt.

[24] Applied computational fluid dynamics, lecture 7 - meshing. ANSYS Inc, 2002. Instructor: André Bakker.

[25] Orthogonal quality. https://allaboutcfd-tomersblog.com/2019/02/01/know-thy-mesh-mesh-quality-part-i/, Accessed November 11, 2020.

[26] Mesh independence study. https://www.computationalfluiddynamics.com.au/convergence-and-mesh-independent-study/, Accessed November 12, 2020.

[27] Reynolds number regimes. https://www.nuclear-power.net/nuclear-engineering/fluid-dynamics/reynolds-number/reynolds-number-for-pipe-flow/, Accessed October 13, 2020.

[28] Engineering toolbox flows. https://www.engineeringtoolbox.com/laminar-transitional-turbulent-flow-d_577.html, Accessed October 13, 2020.

[29] Turbulence modeling - lecture 6 - introduction to introduction to ansys fluent. ANSYS, December 2010. 13.0 Release.